ADVANCED FUNCTIONAL MATERIALS
www.afm-journal.de

Reversible Lithium Storage with High Mobility at Structural Defects in Amorphous Molybdenum Dioxide Electrode

Jun H. Ku, Ji Heon Ryu, Sun Ha Kim, Oc Hee Han, and Seung M. Oh**

This work demonstrates that structural defects in amorphous metal oxide electrodes can serve as a reversible Li^+ storage site for lithium secondary batteries. For instance, molybdenum dioxide electrode in amorphous form (*a*-MoO_2) exhibits an unexpectedly high Li^+ storage capacity (up to four Li per MoO_2 unit), which is larger by a factor of four than that for the crystalline counterpart. The conversion-type lithiation is discarded for this electrode from the absence of Mo metal and lithium oxide (Li_2O) in the lithiated *a*-MoO_2 electrode and the retention of local structural framework. The sloping voltage profile in a wide potential range suggests that Li^+ ions are inserted into the structural defects that are electrochemically nonequivalent. This electrode also shows an excellent cycle stability and rate capability. The latter feature is seemingly due to a rather opened Li^+ diffusion pathway provided by the structural defects. A high Li^+ mobility is confirmed from nuclear magnetic resonance study.

1. Introduction

The consumer market of lithium-ion batteries has been grown as the power sources for small electronic devices until now, but seems to be further expanded to the energy storage devices and electric vehicles in the near future. Despite such a fast market growth, the commercialized electrode materials are still limited to a few highly crystalline ones (for instance, graphite and $LiCoO_2$). Due to the highly crystalline nature of these materials, the Li^+ storage sites are confined only to the crystallographic sites. It is known that the structural defects in non-graphitic carbons can serve as additional Li^+ storage sites,[1–3] but little attention has been paid to the possible Li^+ storage at defect sites in metal oxide electrodes.

Metal oxides have been exploited as the negative electrode for lithium secondary batteries, in which the charging (lithiation) reactions proceed by a co-injection of Li^+ ions and electrons. For lithiation, metal oxides should thus carry the hosts for both Li^+ ions (Li^+ storage sites) and electrons (redox centers). The lithiation mechanism in metal oxide electrodes is classified into two; conversion and insertion reaction. In the former, the metal-oxygen bonds are broken and the metal ions (redox centers) are reduced to their elemental states by taking the injected electrons, while the co-injected Li^+ ions being converted into lithium oxide (Li_2O).[4] Here, Li^+ storage sites cannot be physically identified as the lattice framework is totally broken. In the insertion-type lithiation reaction, however, Li^+ ions are inserted into crystallographic sites without structural disintegration.[5–8] Hence, Li^+ storage sites are crystallographically well-defined and the site population determines Li^+ storage capacity. Obviously, this structural constraint is rather strict if Li^+ hosts are highly crystalline since the Li^+-accessible crystallographic sites are limited in number, but can be opened if Li^+ ions are hosted by any structural defects populated on surface or bulk of metal oxides. In real, a possible Li^+ storage at surface defects has been proven for the nano-sized TiO_2[9] and $Li_4Ti_5O_{12}$.[10] Furthermore, Li^+ storage in bulk defects (vacancies and void spaces) has been well-documented in the less crystalline carbon hosts.[1–3] As far as the redox centers are concerned in the insertion-type metal oxide electrodes, metal ions are traditionally assumed to be the electron acceptor. However, it has been proposed by first-principles calculations that oxygen atoms can function as a redox center.[11,12] Furthermore, the electron host by inserted Li^+ ions themselves to be pseudo-metallic lithium has been ascertained in amorphous carbon electrodes.[13–15] In short, the traditional assumption on the nature of Li^+ storage sites and redox centers in metal oxide electrodes is now challenged by the emergence of new Li^+ storage sites and new redox centers.

A literature survey reveals that the oxides of early transition metal elements (TiO_2,[5] V_2O_5,[6] and MoO_2[8,16–20]) are lithiated by the insertion reaction, whereas the other ones (for instance, CoO[4] and SnO_2[21]) by the conversion reaction. The decisive factor seems to be, among others, the metal-oxygen bond strength. The former group has a relatively stronger

J. H. Ku, Prof. J. H. Ryu, Prof. S. M. Oh
Seoul National University
Department of Chemical and Biological Engineering
Institute of Chemical Processes
and WCU program of C2E2, 599 Gwanak-ro,
Gwanak-gu, Seoul, 151-744, Korea
E-mail: seungoh @snu.ac.kr
S. H. Kim
Korea Basic Science Institute
Daegu Center, Daegu, 702-701, Korea
Prof. O. H. Han
Korea Basic Science Institute
Daegu Center, Daegu, 702-701, Korea
Chungnam National University
Graduate School of Analytical Science & Technology
Daejeon, 305-764, Korea
E-mail: ohhan@kbsi.re.kr

DOI: 10.1002/adfm.201102669

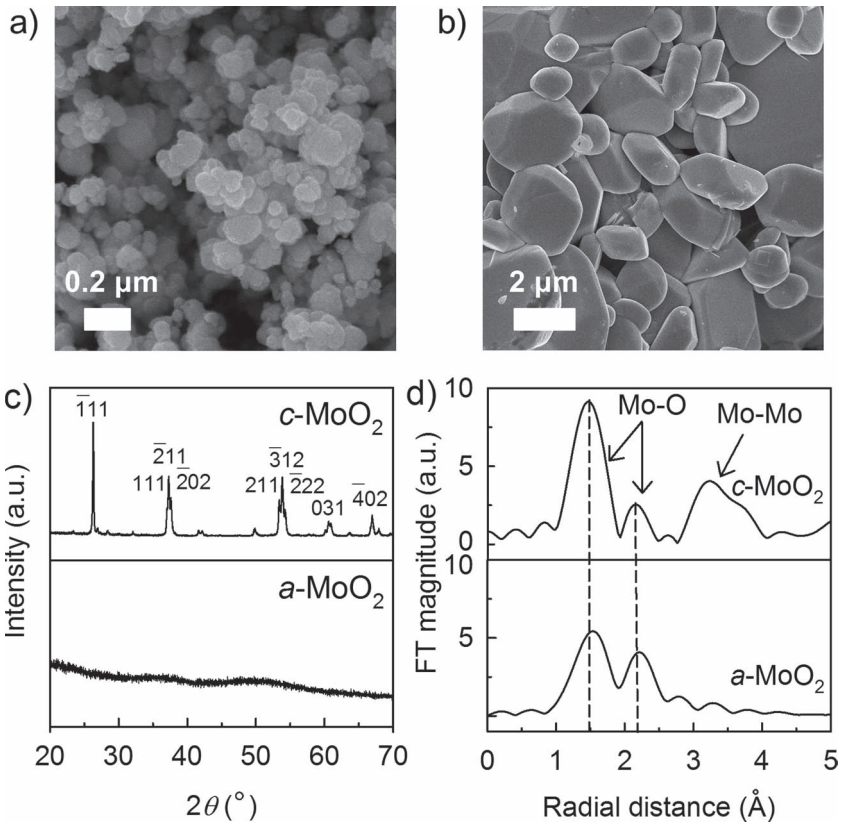

Figure 1. FE-SEM image: a) a-MoO_2 and b) c-MoO_2. c) XRD patterns of c-MoO_2 and a-MoO_2 powder, and d) Fourier transformed $\chi(k)$ of c-MoO_2 and a-MoO_2 powder.

metal-oxygen bond (bond dissociation energy of Mo-O in MoO_2 = 678 kJ mol^{-1} vs. 368 kJ mol^{-1} for Co-O in CoO),[22] such that the lithiation proceeds by the insertion reaction without bond cleavage at ambient temperature. Molybdenum dioxide in its crystalline form belongs to the former group, such that Li^+ ions are inserted only into the crystallographically defined sites. In this work, structural defects are introduced by preparing it as an amorphous form, on which the nature of Li^+ storage sites and redox centers is examined. Another beneficial effect to be assumed with amorphous Li^+ hosts is that solid-state Li^+ diffusion is faster through the rather opened vacancies and void spaces. To confirm this, the mobility of inserted Li^+ ions is assessed by using ^{7}Li nuclear magnetic resonance (NMR) technique.

2. Results and Discussion

Figure 1 shows the powder characteristics of the amorphous molybdenum dioxide (a-MoO_2) and crystalline counterpart (c-MoO_2). The average particle size of a-MoO_2 is *ca.* 0.1 μm as seen in the field-emission scanning electron microscopy (FE-SEM) image (Figure 1a). The annealing of a-MoO_2 leads to a particle growth (Figure 1b). The X-ray diffraction (XRD) pattern of c-MoO_2 in Figure 1c is well-matched with that of the monoclinic MoO_2 phase (space group = $P2_1/c$, JCPDS no. 032-0671). The less-crystalline or amorphous nature of a-MoO_2 is confirmed from the absence of x-ray diffraction peaks (Figure 1c) and long-range ordering in the extended X-ray absorption fine structure (EXAFS) data (Figure 1d). That is, the Fourier-transformed (FT) peak at 3.17 Å that corresponds to the Mo-Mo distance between the neighboring corner-shared distorted MoO_6 octahedra is evident in c-MoO_2, but absent in the amorphous counterpart.[23] The c-MoO_2 sample shows two characteristic FT peaks at 1.47 and 2.15 Å, which correspond to three Mo-O bonds within the distorted MoO_6 octahedra.[23] Note that the peaks for two shorter Mo-O bonds are overlapped to give a broad peak at 1.47 Å, whereas the other longer one at 2.15 Å. As listed in **Table 1**, the FT peaks for two Mo-O bonds appear at the high r space (1.53 and 2.20 Å) for a-MoO_2, reflecting that the MoO_6 octahedra themselves are slightly expanded as compared with those for c-MoO_2.

The electrochemical performances are compared for the c-MoO_2 and a-MoO_2 electrode in **Figure 2**. The c-MoO_2 electrode reversibly takes/releases ca. one Li^+/electron per MoO_2 unit in accordance with the literatures, in which the insertion-type lithiation has been well-documented for c-MoO_2.[5,19] The major lithiation/de-lithiation takes place at the voltage plateau region (1.0 ~ 1.6 V), implying that Li^+ storage sites are well-defined to give the discrete lithiation potential. The amorphous counterpart (a-MoO_2) shows a far different voltage profile. The voltage plateau is diminished to give a rather sloping profile in the whole potential range, indicating that the Li^+ storage sites are not discrete and electrochemically nonequivalent. The first lithiation capacity of a-MoO_2 amounts to 1035 mA h g^{-1} but the de-lithiation capacity is 810 mA h g^{-1} due to the irreversible capacity that is caused by solid electrolyte interphase (SEI) formation and/or Li^+ trapping inside the a-MoO_2 matrix.[24] The reversible Li^+ uptake/removal capacity amounts to four Li/Mo and this value is retained in the continuing cycles with an excellent stability (Figure 2b). As shown

Table 1. The local structural parameter (radial distance) derived from the EXAFS data shown in Figure 1d and 4a.

a-MoO2	Shell	R(Å)	c-MoO2	Shell	R(Å)
OCV	Mo-O	1.53	OCV	Mo-O	1.47
	Mo-O	2.20		Mo-O	2.15
1.0 V/25 °C	Mo-O	1.59	0.01 V/85 °C	Mo-O	-
	Mo-O	2.24		Mo-Mo	2.45
0.5 V/25 °C	Mo-O	1.59			
	Mo-O	2.24			
0.01 V/25 °C	Mo-O	1.57			
	Mo-O	2.24			

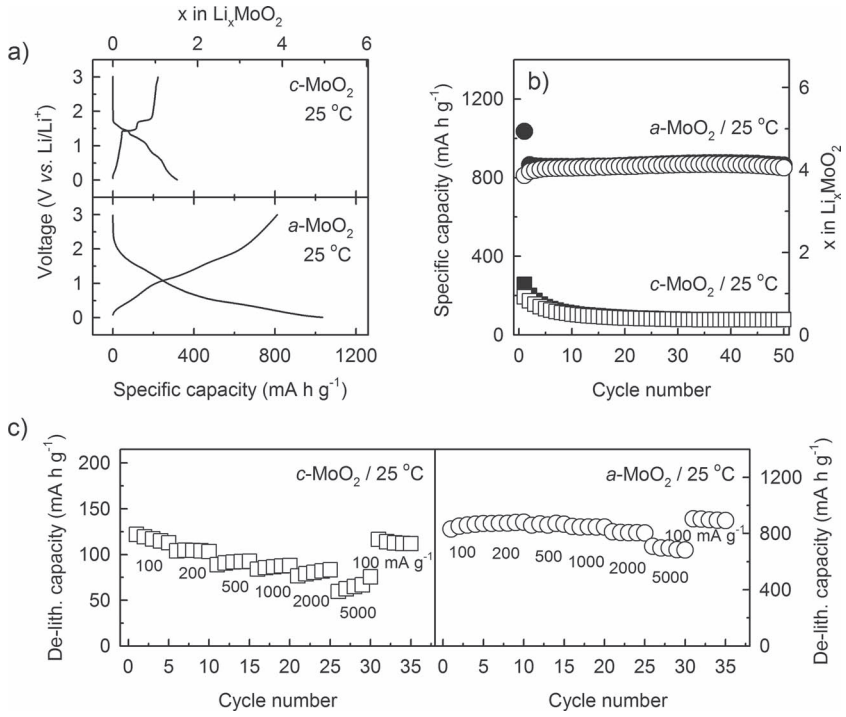

Figure 2. a) The first galvanostatic discharge (lithiation)/charge (de-lithiation) voltage profiles of the *c*-MoO_2/Li and *a*-MoO_2/Li cell. Temp. = 25 °C. Current density = 100 mA g^{-1}. Voltage cut-off = 0.01 ~ 3.0 V (*vs.* Li/Li^+). b) Cycle performance of two cells. The closed symbols are for lithiation and the open ones for de-lithiation. c) Rate performance of *c*-MoO_2/Li and *a*-MoO_2/Li cell. The de-lithiation current density was varied as indicated in the inset, while the lithiation current density being fixed at 100 mA g^{-1}.

in Figure S1 (Supplementary Information), the charge/discharge voltage profiles obtained at the 25th and 50th cycle look similar to each other without evolution of the voltage plateau at 1.0 ~ 1.6 V, which is the signature for the crystalline MoO_2 phase. This reflects that the *a*-MoO_2 matrix is stable under the present electrochemical cycling condition without transition to crystalline phases. The cycling stability is, however, poor for *c*-MoO_2 (Figure 2b). The rate performance is compared for two electrodes in Figure 2c, in which an excellent rate property is noticed for *a*-MoO_2. The de-lithiation capacity of *c*-MoO_2 at a current density of 5000 mA g^{-1} is limited to 55% of the value obtained at 100 mA g^{-1}. In the case of *a*-MoO_2, however, this value amounts to 87%. Moreover, the de-lithiation voltage profile of *a*-MoO_2 at 5000 mA g^{-1} (Figure S2) is not far different to that obtained at 100 mA g^{-1} (Figure 2a). Note that the current density of 5000 mA g^{-1} corresponds to 13 C for graphite electrode (theoretical specific capacity = 372 mA h g^{-1}).

One can suspect that the unexpectedly high reversible capacity (810 mA h g^{-1}) for *a*-MoO_2 results from the conversion-type lithiation since almost the same lithiation capacity is calculated for this reaction ($MoO_2 + 4Li^+ + 4e \rightarrow Mo + 2Li_2O$, theoretical specific capacity = 838 mA h g^{-1}). To discard this possibility, the electrode performance of *c*-MoO_2 that is lithiated by a conversion reaction is discussed in advance. As shown in Figure 2a, the *c*-MoO_2 electrode is lithiated by the insertion reaction at 25 °C. As reported in our previous work,[19] however, the conversion reaction is possible at elevated temperatures (>85 °C) since the Mo-O bond cleavage is now allowed. The most convincing evidence for the conversion reaction in *c*-MoO_2 must be, among others, the formation of metallic Mo and Li_2O. **Figure 3**a presents the Mo 3d X-ray photoelectron spectroscopy (XPS) data and **Table 2** lists the binding energy of Mo 3d photoelectrons emitted from the MoO_2 samples and Mo metal reference. Before cycling (at the open-circuit potential (OCV) = ca. 3.0 V), the *c*-MoO_2 electrode emits the $3d_{5/2}$ and $3d_{3/2}$ photoelectrons at 232.2 and 229.1 eV, respectively, which are the reported values for Mo(IV) oxides.[19] The fully lithiated *c*-MoO_2 (down to 0.01 V) does not emit these photoelectrons, but the other ones of a lower binding energy. As a reference, the XPS data of metallic Mo is presented in Figure 3a, from which it is clear that the fully lithiated *c*-MoO_2 carries the metallic state of Mo (Table 2). The XPS spectrum obtained after a full de-lithiation (up to 3.0 V) is very close to that obtained at OCV. Unambiguously, *c*-MoO_2 is reduced to the metallic state upon lithiation but restored back to Mo(IV) oxide after de-lithiation, which is what is expected for the conversion reaction. The formation of Li_2O is also confirmed on the O 1s spectra shown in Figure 3b. The spectrum obtained after lithiation (0.01 V) is deconvoluted with three peaks. The broad peaks at 531.6 and 534 eV are assigned to those for the carbon-oxygen species (–CO_2 and–CO_3) that are deposited by electrolyte decomposition.[25] The Li_2O formation is ensured by the O 1s peak at 528.8 eV.[26] Furthermore, the O 1s photoelectrons emitted from the oxygen atoms in *c*-MoO_2 are absent at 530 eV in the lithiated sample (0.01 V), manifesting itself that *c*-MoO_2 is disintegrated into metallic Mo and Li_2O. The restoration back

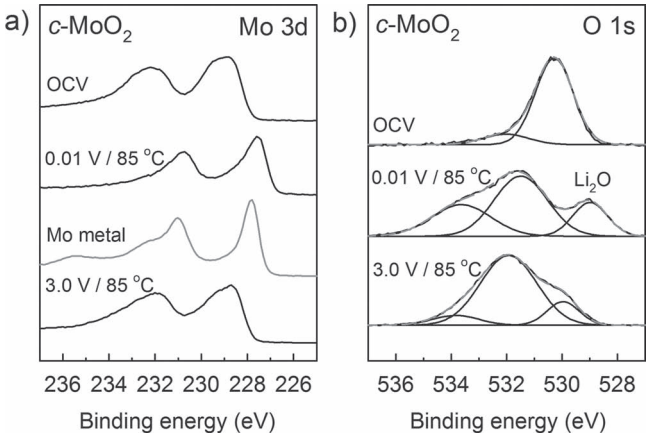

Figure 3. XPS data of the *c*-MoO_2 electrode cycled at 85 °C: a) Mo 3d XPS data. The XPS data of Mo metal is provided as a reference. b) O 1s XPS data. The discharge/charge was made with the *c*-MoO_2/Li cell. Current density = 100 mA g^{-1}. Voltage cut-off = 0.01 ~ 3.0 V (*vs.* Li/Li^+).

Table 2. The binding energy of Mo 3d photoelectrons derived from the XPS data shown in Figure 3a and 4c.

Sample	Mo 3d3/2(eV)	Mo 3d5/2(eV)
c-MoO2/OCV	232.2	229.1
c-MoO2/0.01 V/85 °C	230.9	227.7
Mo metal	231.0	227.8
a-MoO2/OCV	232.3	229.2
a-MoO2/0.01 V/25 °C	231.3	228.1

to Mo(IV) oxide upon de-lithiation (up to 3.0 V) can be confirmed by the appearance of the peak at 530 eV. The intensity of this peak is, however, lower than that observed at OCV since the electrode surface is covered by the electrolyte decomposition products.

From now on, two convincing evidences for *a*-MoO_2 to be lithiated by the insertion reaction are provided in order. First, neither Mo metal nor Li_2O forms even after a full lithiation of *a*-MoO_2. Namely, an intense FT peak corresponding to the Mo-Mo metallic bond develops at 2.45 Å in the EXAFS data acquired from the *c*-MoO_2 electrode lithiated at 85 °C (**Figure 4**a and Table 1), which is the result of Mo metal formation by the conversion reaction. This peak is, however, absent in any FT profiles obtained from the *a*-MoO_2 samples. Meanwhile, the absence of O 1s peak at 528.8 eV in the XPS data of the fully lithiated (0.01 V) *a*-MoO_2 electrode confirms that Li_2O is not generated in *a*-MoO_2 (Figure 4d). Second, the FT peaks for two Mo-O bonds within the distorted MoO_6 octahedra are still observed in the EXAFS data taken from the lithiated *a*-MoO_2 electrode (Figure 4a), indicating that the Mo-O bonds are not broken. However, the increase of Mo-O bonds (Table 1) and the steady decrease in the FT peak intensity with an increase of lithiation suggest that the local framework of MoO_6 octahedra is somewhat disturbed by an uptake of Li^+ ions and electrons. In short, the aforementioned experimental results strongly suggest that *a*-MoO_2 is not lithiated by the conversion reaction at 25 °C, even if its lithiation capacity is very close to the calculated value for the conversion reaction. As discussed, *c*-MoO_2 is lithiated only to one Li/MoO_2 at 25 °C due to the crystallographic constraint. The lithiation capacity of *a*-MoO_2 is enlarged by a factor of four without Mo-O bond cleavage. Only way to account for this enlarged capacity is the Li^+ storage at the structural defects in *a*-MoO_2. The structural defects are numerous to host such a large amount of Li^+ ions, but the defects are electrochemically non-equivalent to give a wide range of lithiation potential (Figure 2a). In order to ensure the Li^+ storage at the structural defects, a separate experiment was made with a series of ball-milled *c*-MoO_2 samples. As shown in Figure S3, the reversible Li^+ storage capacity increases with an increase in the ball-milling time, reflecting that the structural defects that are generated by mechanical impact during the high-energy ball-milling are responsible for the enlarged capacity. Detailed aspects on this will be presented elsewhere. A variety of structural defects can be assumed in *a*-MoO_2; vacancies, void spaces, cluster gaps and interstitial sites. However, the detailed discussion on the nature of structural defects, their population, and their lithiation potential is beyond the scope of this work.

In order for *a*-MoO_2 to accommodate up to four Li^+ ions per formula unit, the equivalent amount of electrons should be hosted by any redox centers. Simply, Mo^{4+} ions in *a*-MoO_2 are the most probable redox centers. To ascertain this, the change of Mo valence upon lithiation is traced by using Mo K-edge X-ray absorption near-edge structure (XANES) spectroscopy. As shown in Figure 4b and **Table 3**, the Mo K-edge energy shifts to the lower value, upon lithiation (0.01 V), to be close to that for the Mo metal reference. The similar reduction of Mo^{4+} ions is confirmed on the Mo 3d XPS data (Figure 4c), in which the binding energy of Mo 3d photoelectrons decreases upon lithiation to be close to that for metallic Mo (Table 2). Clearly, the metal ions are the major electron host. One feature not to be ignored in Figure 4b and Table 3 is, however, that the Mo K-edge energy of the fully lithiated *a*-MoO_2 (0.01 V) is still higher than that of the Mo metal reference, indicating that Mo valence is still higher than zero. Moreover, the Mo K-near-edge (XANES) spectrum of this sample is not perfectly

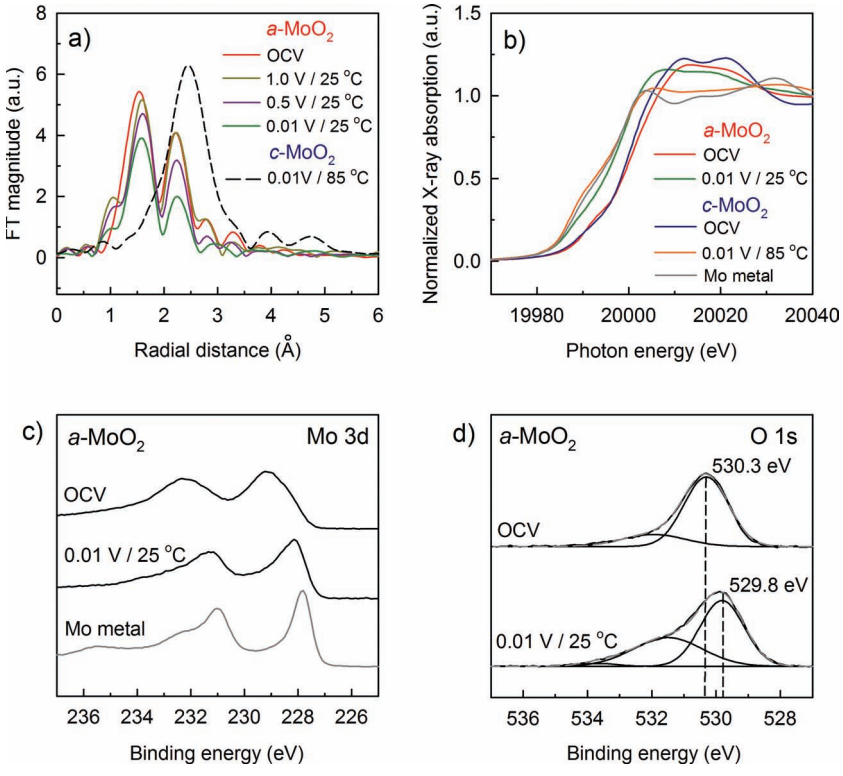

Figure 4. XAS and XPS data of *a*-MoO_2 electrode cycled at 25 °C. a) Fourier transformed $\chi(k)$ obtained with lithiation. As a reference, the result obtained with *c*-MoO_2 after a full lithiation at 85 °C is provided. b) Normalized Mo K-edge XANES spectra for the *a*-MoO_2 and *c*-MoO_2 electrode. c) Mo 3d XPS data. The XPS data of Mo metal is provided as a reference. d) O 1s XPS data.

Table 3. The Mo K-edge energy at the peak edge step and the edge shift (from Figure 4b)

Sample	Edge energy/eV	Edge shift/eV
a-MoO_2/OCV	20012.5	8.9
a-MoO_2/0.01 V/25 °C	20008.2	4.6
c-MoO_2/ OCV	20012.0	8.4
c-MoO_2/0.01 V/85 °C	20004.3	0.7
Mo metal	20003.6	-

matched with that of Mo metal (Figure 4b). Note, however, that the XANES spectrum of the lithiated *c*-MoO_2 is closely matched with that for the Mo reference due to a formation of metallic Mo (Figure 4b). The Mo valence of higher than zero is further ascertained in the Mo 3d XPS data (Figure 4c). The binding energy of Mo $3d_{5/2}$ and $3d_{3/2}$ photoelectrons that are emitted from the lithiated *a*-MoO_2 (0.01 V) is slightly higher than that for the Mo metal reference (Table 2). This is somewhat puzzling since the Mo valence should be zero if the Mo^{4+} ions take four electrons per MoO_2 unit. If four electrons are not accepted by the Mo^{4+} ions, the remnant electrons should be hosted by other redox centers. Along this line, a marginal but not to be ignored electron host by oxygen species is proposed in this work. Namely, the binding energy of O 1s photoelectrons (529.8 eV) emitted from the fully lithiated *a*-MoO_2 (0.01 V) is slightly lower than that emitted from the initial *a*-MoO_2 sample (530.3 eV), manifesting itself that the electron density on the oxygen atoms increases to some degree upon lithiation (Figure 4d). However, the nature of oxygen species that are responsible for electron host is not clear. In this work, the electron host by the inserted Li^+ ions is discarded from the NMR study. The magic angle spinning (MAS) ^{7}Li NMR spectra (**Figure 5**a and 5c) illustrate that the chemical shift of ^{7}Li nuclei varies within a narrow range (~3 ppm) near 0 ppm, indicating that the inserted lithium species are not metallic but their oxidation state is close to +1. More evidently, the peak near 263 ppm is absent (Figure 5a), which is known for the metallic lithium species.[27,28]

The NMR data in Figure 5 give a further insight into the nature of Li^+ storage sites and mobility of inserted Li^+ ions in two electrodes. A single broad peak appears in the center peak region of MAS spectra taken from *a*-MoO_2 (Figure 5c), whereas one sharper peak with a few weaker ones from *c*-MoO_2 (Figure 5d). The spectral difference between two samples supports the model of Li^+ storage sites proposed in this work; a few well-defined discrete sites for *c*-MoO_2 and a wide distribution of Li^+ storage sites in *a*-MoO_2. It is also noted in Figure 5c that the center peak for *a*-MoO_2 gradually shifts to the higher frequency (the larger chemical shift value) with an increase in Li^+ insertion without appearance of new peaks. This suggests a delocalization of electrons in the *a*-MoO_2 matrix and a rapid motion of the inserted lithium species.[27,28] That is, the inserted lithium species move from one site to another fast enough to give a broad single peak near 0 ppm in *a*-MoO_2. Such a site-exchange is, however, slow in *c*-MoO_2 to give the resolved sharper peaks. This mobility difference is further ascertained by the variable-temperature NMR experiments.

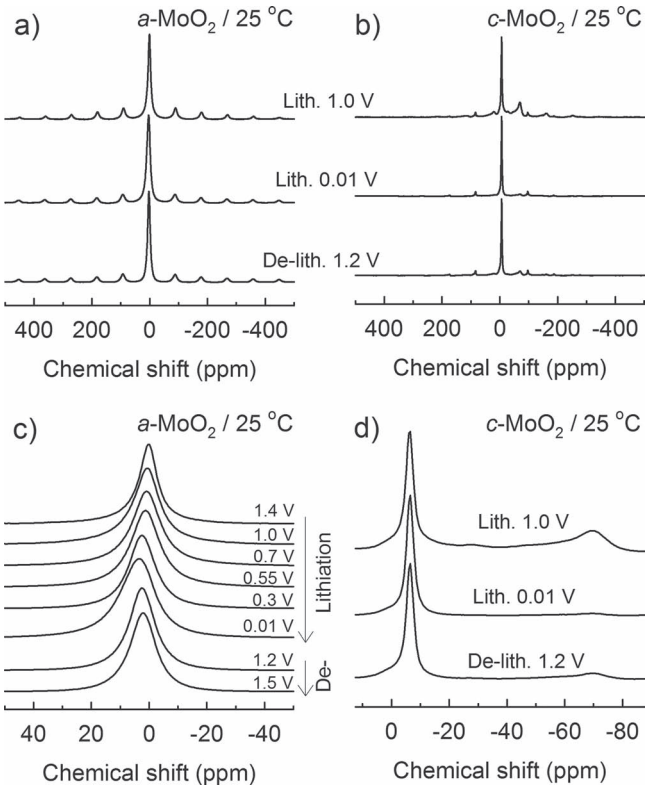

Figure 5. The wide spectral range of MAS data as a function of lithiation/de-lithiation at 25 °C: a) *a*-MoO_2 and b) *c*-MoO_2. The expanded view for the center peak region: c) *a*-MoO_2 and d); *c*-MoO_2. The sample spinning rate was 14 kHz. The spectra were plotted in the same intensity scale without calibration in terms of the lithium content in the sample or the number of NMR acquisition.

The static ^{7}Li NMR spectra obtained from the fully lithiated *a*-MoO_2 sample show that the center peak becomes narrower with an increase in temperature (**Figure 6**a), reflecting that the site-exchanging rate is in a NMR time scale (10^{-4} ~10^{-5} s). This feature is further confirmed on the variable-temperature MAS spectra (Figure 6b), in which the center peak becomes broader with an increase in temperature. This is a commonly observed phenomenon when the motion of lithium species is coupled by the artificial motion (sample spinning).[29,30] This implies that the site-exchanging rate of inserted lithium in *a*-MoO_2 is similar to the spinning rate (7 kHz), corresponding to a correlation time in the order of ~10^{-4} s. In contrast, a much slower lithium motion in *c*-MoO_2 is evident from the observations that the linewidth of center peak near 0 ppm does not change in both the static (Figure 6c) and MAS spectra (Figure 6d) obtained from the fully lithiated *c*-MoO_2 electrode. This mobility difference can explain the difference in rate capability for two electrodes by taking into account that the solid-state Li^+ diffusion is the slowest process in charge/discharge reactions. The higher rate capability for *a*-MoO_2 (Figure 2c) is likely due to the higher mobility of inserted lithium species. The rather opened Li^+ pathways provided by the structural defects may explain this favorable feature.

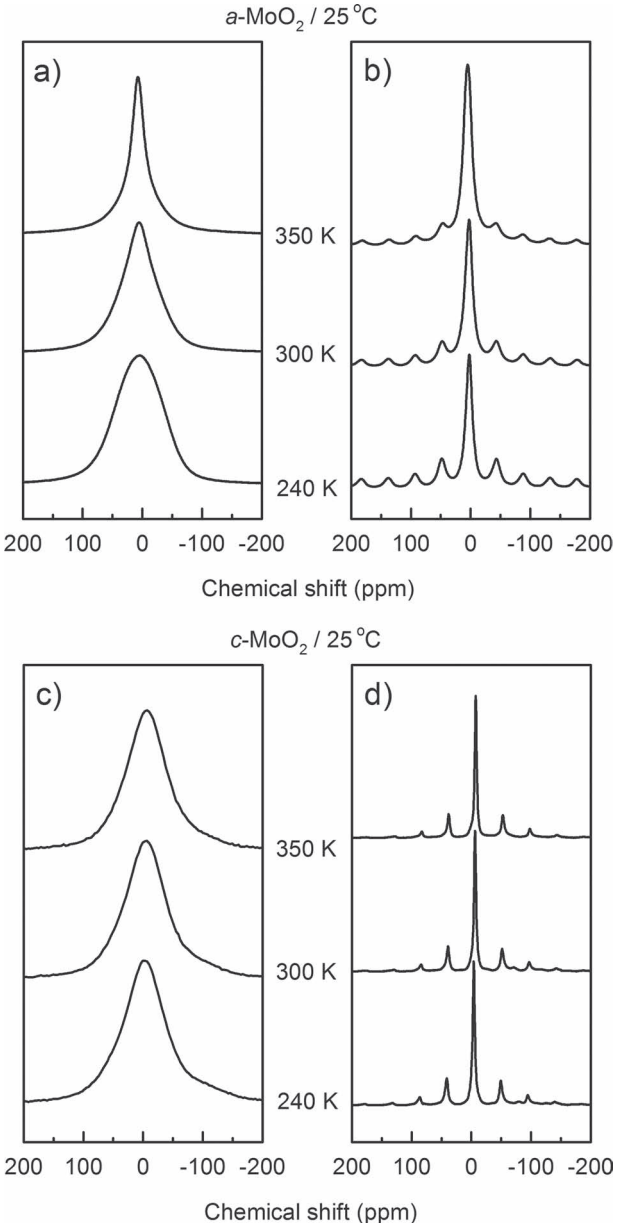

Figure 6. The variable-temperature ^{7}Li NMR spectra for the fully lithiated (down to 0.01 V at 25 °C) *a*-MoO_2 and *c*-MoO_2 electrode: a) The static spectra for *a*-MoO_2. b) The MAS spectra for *a*-MoO_2. c) The static spectra for *c*-MoO_2. d) The MAS spectra for *c*-MoO_2. The spinning rate was 7 kHz. The spectra were plotted in the same intensity scale without calibration in terms of the lithium content in the sample or the number of NMR acquisition.

3. Conclusion

The nature of Li^+ hosting sites in *a*-MoO_2 has been assigned to the structural defects. Unexpectedly, the structural defects act as a stable Li^+ storage site to give a very stable cycle performance. The mobility of inserted lithium species is high in *a*-MoO_2 to give a high rate capability. This work demonstrates that the structural defects in metal oxide electrodes, to which little attention has been paid, can be an important Li^+ host. Defects are not confined to metal oxides, but ubiquitous in solids. Continuing research on the structural defects in other metal oxides, phosphates, fluorides and Li alloying materials as a Li^+ hosting site may lead to a discovery of new electrode materials of high capacity and high rate capability.

4. Experimental Section

Synthesis: The *a*-MoO_2 powder was synthesized by modifying the reported procedure, which is based on the reduction of aqueous Mo^{6+} solution by a reducing agent.[16] In detail, 50 mL of 0.25 M K_2MoO_4 solution was prepared by dissolving K_2MoO_4 in distilled water, into which 50 mL of 2.5 M KBH_4 solution (reducing agent) that was separately prepared by dissolving KBH_4 in dilute KOH solution (pH = 11) was slowly added using a syringe pump. The reaction mixture was vigorously stirred while maintaining pH = 2.0 by adding concentrated HCl. The resulting precipitate was filtered and washed with distilled water, which was followed by drying at 80 °C for overnight and 300 °C under vacuum for 2 h to obtain the *a*-MoO_2 powder. The *c*-MoO_2 powder was obtained by annealing the *a*-MoO_2 powder at 900 °C in argon atmosphere.

Spectroscopic characterizations: The particle morphology was examined using a FE-SEM (JEOL JSM-6700F). The X-ray diffraction patterns were obtained using a D8-Bruker diffractometer equipped with Cu K_α radiation (1.54056 Å). The XRD patterns were recorded at 40 kV and 40 mA using a continuous scanning mode with 5.0 degree min^{-1}. The XPS measurements were made in an UHV multipurpose surface analysis system (SIGMA PROBE, Thermo, UK) using an Al K_α (1486.6 eV) anode operating at constant power (15 kV and 10 mA). The binding energy scale was calibrated from the hydrocarbon contamination using the C 1s peak at 285 eV. The Mo K-edge XANES and EXAFS data were obtained at the Pohang Light Source (PLS) with a ring current of 120–170 mA at 2.5 GeV. Data were collected in a transmission mode using gas-filled ionization chambers (30% nitrogen and 70% argon) as detectors. A Si (111) monochromator crystal was used with detuning to 80% in intensity to eliminate the high-order harmonics. Energy calibration for Mo K-edge was carried out using Mo metal powder. The static and MAS ^{7}Li NMR experiments were made at 9.4 T on Bruker Avance II$^+$ 400 MHz NMR system. Prior to the sample transfer to a rotor (4 mm outer diameter) in a glove box, the electrode materials were washed with DMC and dried in an argon-filled dry box. For the MAS and static spectra, an excitation pulse length of 1 μs (with a 90° flip pulse length of 2.2 μs), a pulse repetition delay of 3 s, and the number of acquisition of 128 or 256 were employed. For MAS spectra, the samples were spun at 14 kHz at room temperature but 7 kHz at higher or lower temperature. Chemical shift was referenced to the external saturated LiCl aqueous solution.

Electrochemical characterizations: The working electrodes were prepared by coating the slurry of MoO_2 powder, Super-P and polyvinylidene fluoride (PVdF) (7:2:1 in wt. ratio) on a piece of Cu foil. The electrode plates were heated under argon flow at 300 °C for 12 h. The electrochemical performances were evaluated using a two-electrode 2032-type coin cell, in which a round disk of the working electrode (diameter = 1.1 cm and MoO_2 loading = 2.0 mg) was placed along with Li foil counter electrode. To avoid spectroscopic interferences that may come from the carbon additive and polymer binder in the XPS measurement, the working electrodes that are free from Super-P and PVdF were prepared by spreading the MoO_2 powder onto a piece of Ni foam and pressing at 100 Mpa. Different electrolytes were used according to the working temperature; 1.0 M $LiPF_6$ dissolved in a mixture of ethylene carbonate (EC) and dimethyl carbonate (DMC) (1:2 v/v) at 25 °C and 0.7 M lithium bis(oxalatoborate) (LiBOB) in a mixture of ethylene carbonate (EC) and diethyl carbonate (DEC) (1:1 v/v) at 85 °C. As the separator, porous polypropylene (PP) film was used at 25 °C but a glass fiber sheet at 85 °C since PP separator is deformed at >85 °C.

Supporting Information

Supporting Information is available from the Wiley Online Library or from the author.

Acknowledgements

This work was supported by National Research Foundation of Korea funded by the MEST (R31-10013 and NRF-2010-C1AAA001-2010-0029065).

Received: November 7, 2011
Revised: April 23, 2012
Published online: May 18, 2012

[1] J. R. Dahn, T. Zheng, Y. Liu, J. S. Xue, *Science* **1995**, *270*, 590.
[2] Z. Ogumi, M. Inaba, *Bull. Chem. Soc. Jpn* **1998**, *71*, 521.
[3] C. H. Park, S. Yoon, S. I. Lee, S. M. Oh, *Carbon* **2000**, *38*, 995.
[4] P. Poizot, S. Laruelle, S. Grugeon, L. Dupont, J.-M. Tarascon, *Nature* **2000**, *407*, 496.
[5] T. Ohzuku, T. Kodama, T. Hirai, *J. Power Sources* **1985**, *14*, 153.
[6] B. Y. Liaw, I. D. Raistrick, R. A. Huggins, *Solid State Ionics* **1991**, *45*, 323.
[7] K. M. Colbow, J. R. Dahn, R. R. Haering, *J. Power Sources* **1989**, *26*, 397.
[8] J. R. Dahn, W. R. McKinnon, *Solid State Ionics* **1987**, *23*, 1.
[9] W. J. H. Borghols, M. Wagemaker, U. Lafont, E. M. Kelder, F. M. Mulder, *Chem. Mater.* **2008**, *20*, 2949.
[10] W. J. H. Borghols, M. Wagemaker, U. Lafont, E. M. Kelder, F. M. Mulder, *J. Am. Chem. Soc.* **2009**, *131*, 17786.
[11] G. Ceder, Y.-M. Chiang, D. R. Sadoway, M. K. Aydinol, Y.-I. Jang, B. Huang, *Nature* **1998**, *392*, 694.
[12] K. E. Swider-Lyons, C. T. Love, D. R. Rolison, *Solid State Ionics* **2002**, *152–153*, 99.
[13] N. Takami, A. Satoh, M. Oguchi, H. Sasaki, T. Ohsaki, *J. Power Sources* **1997**, *68*, 283.
[14] S. Wang, H. Matsui, H. Tamamura, Y. Matsumura, *Phys. Rev. B* **1998**, *58*, 8163.
[15] K. Guerin, M. Menetrier, A. Fevrier-Bouvier, S. Flandrois, B. Simon, P. Biensan, *Solid State Ionics* **2000**, *127*, 187.
[16] A. Manthiram, C. Tsang, *J. Electrochem. Soc.* **1996**, *143*, L143.
[17] Y. Liang, S. Yang, Z. Yi, X. Lei, J. Sun, Y. Zhou, *Mater. Sci. Eng. B* **2005**, *121*, 152.
[18] X. Ji, P. S. Herle, Y. Rho, L. F. Nazar, *Chem. Mater.* **2007**, *19*, 374.
[19] J. H. Ku, Y. S. Jung, K. T. Lee, C. H. Kim, S. M. Oh, *J. Electrochem. Soc.* **2009**, *156*, A688.
[20] Y. Shi, B. Guo, S. A. Corr, Q. Shi, Y. S. Hu, K. R. Heier, L. Chen, R. Seshadri, G. D. Stucky, *Nano Letters* **2009**, *9*, 4215.
[21] I. A. Courtney, J. R. Dahn, *J. Electrochem. Soc.* **1997**, *144*, 2045.
[22] B. deB. Darent, *National Standard Reference Data Series: National Bureau of Standards* No. 31, Washington **1970**.
[23] T. Ressler, O. Timpe, T. Neisius, J. Find, G. Mestl, M. Dieterle, R. Schroegl, *J. Catalysis* **2000**, *191*, 75.
[24] S. Laruelle, S. Grugeon, P. Poizot, M. Dolle, L. Dupont, J.-M. Tarascon, *J. Electrochem. Soc.* **2002**, *149*, A627.
[25] R. Dedryvere, S. Laurelle, S. Grugeon, P. Poizot, D. Gonbeau, J. M. Tarascon, *Chem. Mater.* **2004**, *16*, 1056.
[26] S. Tanaka, M. Taniguchi, H. Tanigawa, *J. Nucl. Mater.* **2000**, *283*, 1405.
[27] M. Letellier, F. Chevallier, C. Clinard, E. Frackowick, J.-N. Rouzaud, F. Béguin, *J. Chem. Phys.* **2003**, *118*, 6038.
[28] M. Letellier, F. Chevallier, F. Béguin, E. Frackowick, J.-N. Rouzaud, *J. Phys. Chem. Solids* **2004**, *65*, 245.
[29] F. Lauprêtre, *High-resolution ^{13}C NMR investigations of local dynamics in bulk polymers at temperatures below and above the glass transition temperature: NMR basic principles and progress*, Springer-Verlag, Berlin **1994**.
[30] E. Brunner, *J. Chem. Soc., Faraday Trans.* **1990**, *86*, 3957.